Chapter 4

Relative Contributions of Electron and Energy Transfer in Nanoparticle-Fluoroprobe Systems

Relative Contributions of Electron and Energy Transfer in Nanoparticle-Fluoroprobe Systems

4.1. Introduction

In recent years, there has been a great deal of research endeavors to investigate the photophysical aspects of multicomponent nanostructured assemblies arising from the invasive integration of molecular probes and metallic nanostructures that mimics many ubiquitous processes in materials and life sciences.[1-4] The ability of metal nanostructures in manipulating and guiding light at the nanometer length scale and therefore, to modulate the fluorescence emission of vicinal fluoroprobes has propelled their widespread interest in fluorescence-based sensing in biology and nanophotonics technologies.[5-7] Noble metal particles, *viz.*, copper, silver and gold, in the nanometer size regime exhibit strong absorption in the visible region and this is, indeed, a small particle effect since they are absent in the individual atom as well as in their bulk.[8] The time-varying electric field of the electromagnetic radiation causes collective oscillation of the conduction electrons in metal nanoparticles with a resonance frequency, often coined as localized surface plasmon resonance (LSPR).[9] These collective oscillations of the conduction band electrons enable strong optical absorption and scattering in the subwavelength structures, with spectral properties dependent upon size, shape, interparticle interactions, dielectric properties and local environment around the nanoparticles.[10] The localized surface plasmon resonances of metallic nanostructures imbue significant influences on the photophysical properties of organic fluoroprobes in the close vicinity of the conducting metal surfaces and therefore, the field of plasmonics imparts considerable impact in biophotonics through radiative decay engineering.[11-13] To meet the challenges that lie ahead, the understanding of plausible interactions in nanoparticle-fluoroprobe hybrid assemblies is essential before miniaturizing them into devices.[14]

Since, fluorescence spectroscopy is a very sensitive technique, there is a growing recognition in understanding the physicochemical aspects of the molecule-surface interactions of fluorescent probes attached onto the surface of noble metal

nanoparticles.[15] For these studies, silver nanoparticles have been of interest as, compared with gold, the silver plasmon band is more sensitive to chemical modifications of the surface upon adsorption of nucleophile or electron donors.[16] Moreover, the plasma frequency of silver nanoparticles in the visible region overlaps with the emission wavelength of usual energy donors.[17] Therefore, fluorophore-bound silver nanoparticles provide a convenient way to examine the mechanistic details of various de-excitation pathways of the photoexcited fluoroprobes, such as, energy and electron transfer to the bound nanoparticles. Photoinduced electron transfer (PET), in which a charge transfer complex is formed between an electron donor and an electron acceptor that can return to the ground state without emission of a photon, is one of the pathways of de-activation of the excited probe molecules leading to quenching of fluorescence intensity of the molecular probes. Förster resonance energy transfer (FRET), where the donor molecule absorbs a photon and there is an accepter molecule close to the donor molecule, radiationless energy transfer can occur from the donor to the acceptor resulting in a decrease of the fluorescence intensity and lifetime of the donor molecule.

Although, the photophysical aspects of molecular probes near metallic nanostructures have extensively been investigated, there have been fewer experimental investigations on spectroscopic properties of pyrene moieties attached onto the surface of metallic nanoparticles. Rotello and colleague[18] have reported the fabrication of multivalent colloid-based receptors as well as dynamic systems based on nanoparticle scaffolds in which the migration of alkanethioate ligands with pyrene units has been suggested upon the addition of guest molecules. George Thomas and Kamat[19] have reported the engineering of thiol-capped gold nanocluster surfaces with 1-aminoethylpyrene and demonstrated that fluorescence intensity can be enhanced order of magnitude due to transfer of lone pair of electrons from the molecular probes to the gold nanoparticles when the organic dyes are placed in the vicinity of the metallic particles. Zhu and co-authors[20] have reported the synthesis and photophysical properties of 10-(1-pyrenyl)-6-oxo-decanethiol and 17-(1-pyrenyl)-1-oxo-heptadecanethiol capped gold nanoparticles and unusual fluorescence enhancement was observed upon aging dichloromethane dispersions of these colloidal particles. The findings of this experiment elucidated the role of the chain density gradient and the motion of termini groups of alkanethiolates

adsorbed onto the surface of gold nanoparticles for the fluorescence enhancement. Kamat group[21] have demonstrated the spectroscopic investigation of direct electron transfer between gold nanoparticles and surface bound (1-pyrenyl)-6-oxaheptanethiol molecules induced by pulsed laser irradiation. It has been observed that binding of pyrenethiol directly to the gold nanoparticles results in quenching of singlet excited state and the charge separation is sustained for microsecond before undergoing recombination. Pal and co-workers[22] have studied the fluorescence quenching behavior of aminomethylpyrene near gold nanoparticles in the size range of 8−73 nm; it was elucidated that the quenching efficiency of the metallic nanostructures is not a linear function of the particle size rather than different in the two different size regime of the particles. It was observed that the smaller particles of gold are efficient quenchers of molecular fluorescence than the larger ones which is due to higher surface-to-volume ratio of the small metallic particulates. Therefore, it is, now, well-established that fluorescence of pyrene moieties could be either enhanced or quenched depending on its relative position in the vicinity of noble metal nanostructures. While the fluorescence of molecular probes is quenched, indeed, although the physics behind possible deactivation pathways of the photoexcited fluoroprobe near metal nanostructures is established, the relative contributions of electron and energy transfer processes are of worth investigation.

In this chapter, pyrene and its two amine derivatives have elegantly been employed as fluorescent probes and four different sizes of silver nanoparticles have, judiciously, been selected to study the interactions in metal-fluoroprobe hybrid assemblies. Size-selective silver nanoparticles have been synthesized using sodium borohydride as the reducing agent and trisodium citrate as the reducing as well as capping agent. Since fluorescence spectroscopy is a very sensitive technique, a strong correlation is observed between the observed fluorescence intensity and the photophysical properties of the metal-fluoroprobe hybrid assemblies. It is observed that fluorophore-bound silver nanoparticles provide a convenient way to examine the mechanistic details of various deactivation pathways of photoexcited fluoroprobes, such as, electron and energy transfer to the bound nanoparticles and eventually, paves a substantial avenue in realizing the relativity of electron and energy transfer contributions in nanoparticle-induced fluorescence quenching.

4.2. Experimental

4.2.1. Synthesis of Variable Sizes of Silver Nanoparticles. Four different sets of silver nanoparticles have been synthesized by wet chemical reduction of silver nitrate using sodium borohydride as reducing agent and trisodium citrate as stabilizing agent. A detailed of the synthesis of different sets of silver nanoparticles could be described as follows.

Synthesis of Silver Nanoparticles (Set A). In a typical experiment, 50 mL of 0.25 mM silver nitrate solution was taken in a 100 mL beaker. Then, 2.5 mL 1% trisodium citrate solution was added and stirred vigorously using a magnetic stirrer at 0 0C temperature. After that, approximately, 1 mL of freshly prepared sodium borohydride solution ($AgNO_3$: $NaBH_4$ = 1: 20) was added to the reacting solution at a time and stirring was continued for another 30 min. At this temperature, trisodium citrate does not reduce the silver nitrate solution and only acts as stabilizing agent. The development of yellow coloration indicates the formation of silver nanoparticles.

Synthesis of Silver Nanoparticles (Set B). In the typical synthesis, 50 mL of 0.25 mM silver nitrate solution was taken in a 100 mL beaker. Then, approximately 2.5 mL 1% trisodium citrate solution was added to the reacting solution and mixed, vigorously, by stirring using a magnetic stirrer. Then, approximately, 1 mL of freshly prepared ($AgNO_3$: $NaBH_4$ = 1: 9) sodium borohydride solution was added to the reacting solution at a time at room temperature. At this temperature, trisodium citrate does not reduce the silver nitrate solution further and only acts as stabilizing agent. The reacting mixture was stirred for 30 min. The resulting yellow colored solution indicated the formation of silver nanoparticles.

Synthesis of Silver Nanoparticles (Set C). Another set of silver nanoparticles was synthesized in the same method by only varying sodium borohydride concentration ($AgNO_3$: $NaBH_4$ = 1: 6) and keeping the other conditions and reagents same as set B.

Synthesis of Silver Nanoparticles (Set D). For the synthesis of fourth set of silver nanoparticles, trisodium citrate reduction method was used. In the typical experiment, 50 mL of 0.25 mM silver nitrate solution was taken in a 100 mL beaker and was heated to boiling. To this solution, 1 mL 1% trisodium citrate solution was added at a time and was mixed, vigorously, by stirring using a magnetic stirrer. The reaction was allowed to take

place until the color of the solution changed to greenish yellow. The solution was, then, cooled to room temperature. A lexicon of the synthetic conditions for the preparation of four different sizes of silver nanoparticles has been enunciated in Table 4. 1.

Table 4.1. Synthetic Conditions for the Four Different Sets of Silver Nanoparticles[#]

Set	Vol. of $AgNO_3$ (0.1 M) (mL)	Vol. of citrate (1%) (mL)	Condition	$AgNO_3$: $NaBH_4$	Color	λ_{max} (nm)	Diameter (nm)
A	0.125	2.5	0 ^{0}C	1:20	Yellow	379	2±0.5
B	0.125	2.5	25 ^{0}C	1:9	Yellow	392	6±1
C	0.125	2.5	25 ^{0}C	1:6	Yellow	399	9±2
D	0.125	1.0	100 ^{0}C	-	Greenish yellow	409	21±3

[#]For silver nanoparticle synthesis, the total volume of the solution was 50 mL.

4.2.2. Making Metal-Probe Hybrid Assembly. In a typical set, an aliquot of Ag NPs (0.75─10 µM) from different sets was added to a solution of pyrene or its derivatives (0.03-0.3 µM) and the final volume of the solution was maintained to 5 mL. The pH of all the solutions was adjusted to~7.0. The solution was allowed to incubate for 12 h to complete the surface complexation process and fluorescence of each solution was measured in the spectrofluorimeter.

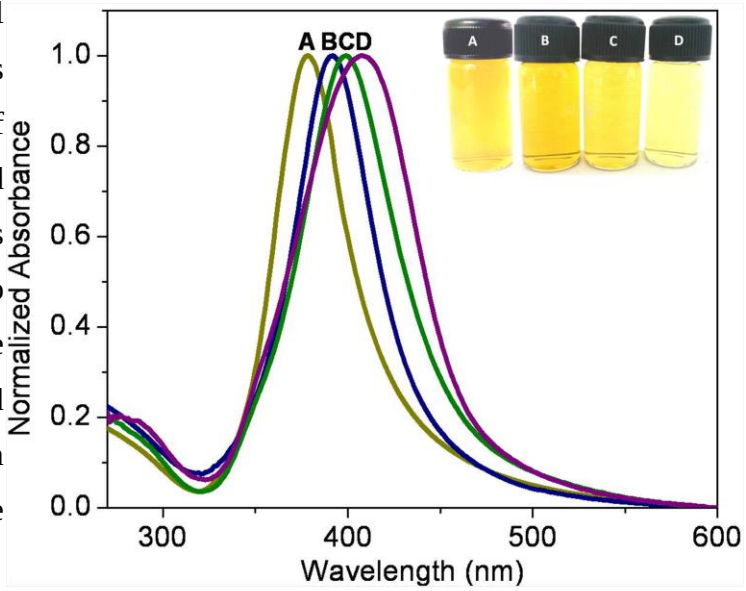

Figure 4.1. (A-D) Normalized UV-visible spectra of silver nanoparticles (50 µM) of variable sizes of sets A-D, respectively. Inset shows the digital photograph of the corresponding silver particles.

4.3. Results and Discussion

The as-synthesized colloidal dispersions of the silver particles have been

characterized by absorption spectroscopy and transmission electron microscopic studies. Figure 4.1 shows the normalized absorption spectra of four different sets of silver colloids. Inset shows the digital camera photograph exhibiting the characteristic colors of four different sets of silver nanoparticles. In the UV-vis spectrum, it is seen that the absorption maximum appears at 379, 392, 399 and 408 nm for silver particles of sets A, B, C and D, respectively. This absorption band arises due to the localized surface plasmon band of spherical silver nanoparticles; for nanoparticles much smaller than the wavelength of light, the electromagnetic field is uniform across a particle such that all the conduction electrons move in-phase producing only dipole-type oscillations that is manifested by a single narrow peak in the LSPR spectrum.[23] Moreover, the shape of the LSPR spectrum is determined by the relative dimension of the particles to that of the incident electromagnetic radiation. It is apparent that the absorption spectrum is red shifted and broadened from sets A to D indicating the gradual increase in size of the silver nanoparticles. This is due to the fact that the observed spectral shift results from the spreading' of particle's surface charge over a larger surface area so that the surrounding medium better compensates the restoring force, thus, showing the electron oscillations.[23]

The morphology, composition, and crystallinity of the as synthesized silver particles are presented in Figure 4.2. Transmission electron micrographs of the representative silver particles (panels a−d) show that the particles are spherical or nearly spherical with average diameter in the range of 2 ± 0.5, 6 ± 1, 9 ± 2, and 21 ± 3 nm for sets A, B, C, and D respectively. The number concentration (number of particles per milliliter of the solution, N) of silver particles can be calculated by taking the ratio of total volume of the atoms to the effective volume of each particle taken in average.[24] The approximate numbers of silver nanoparticles per milliliter of the solution have been calculated using the formula,

$$N = \frac{N_0 C}{1000 f}\left(\frac{r}{R}\right)^3 \qquad (4.1)$$

where, N_0 is the Avogadro number, C the concentration of the silver precursor, f the packing fraction of the atoms in the nanostructures, r the radius of silver atoms, R the average radii of the particles. Assuming the packing fraction as 0.74 for *fcc* silver[25] and a precursor concentration of 0.25 mM, the number concentration of silver particles has been *ca.* 8.33×10^{14}, 3.09×10^{13}, 9.14×10^{12} and 7.19×10^{11} mL^{-1} for sizes 2, 6, 9 and 21 nm respectively. High resolution TEM image (panel e) of the silver particles of set D

exhibits the lattice fringes with an interplanner spacing of ~0.232 nm consistent with (111) plane of silver; the continuous fringe pattern observed in the HRTEM image demonstrates the single crystalline nature of the silver nanoparticles.[26] Selected area electron diffraction (panel f) of the silver particles of set D illustrates four sets of lattice planes with *d* spacings of 2.32, 2.04, 1.44 and 1.22 Å that correspond to the (111), (200), (220), and (311) planes of the face-centered cubic silver particles.[27]

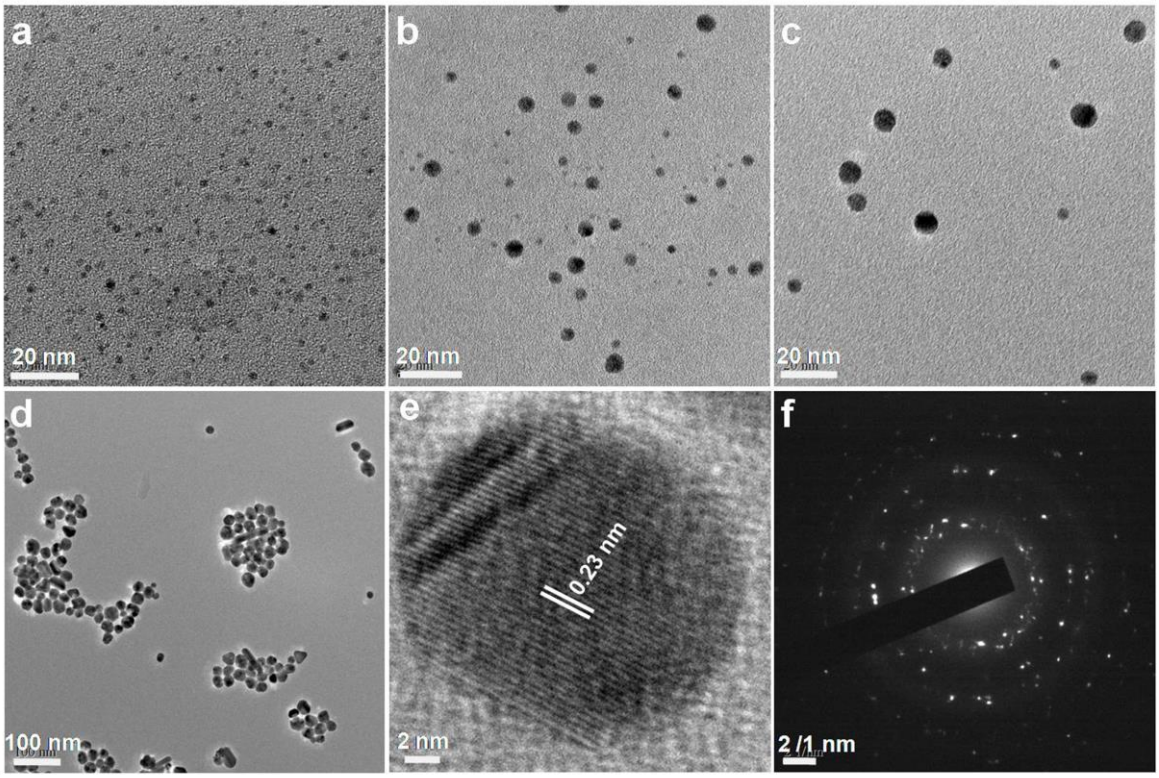

Figure 4.2. (a, b, c, d) Transmission electron micrographs of silver nanoparticles of sets A, B, C and D respectively; (e) high resolution transmission electron micrograph and (f) selected area electron diffraction pattern of set D silver particles.

Pyrene is a polycyclic aromatic hydrocarbon consisting of four fused benzene rings, resulting in a flat aromatic system and is used commercially to make dyes and dye precursors. There have been extensive studies on the photophysics of pyrene: its electronic spectrum and state assignments, kinetic details of excimer formation, spectral pressure effects, photoionization, delayed luminescence, and quasilinear spectra, etc.[28] Due to their numerous well-characterized photophysical and photochemical properties, pyrene[29] and its amine derivatives[30,31] have been widely used as fluorescent probes to

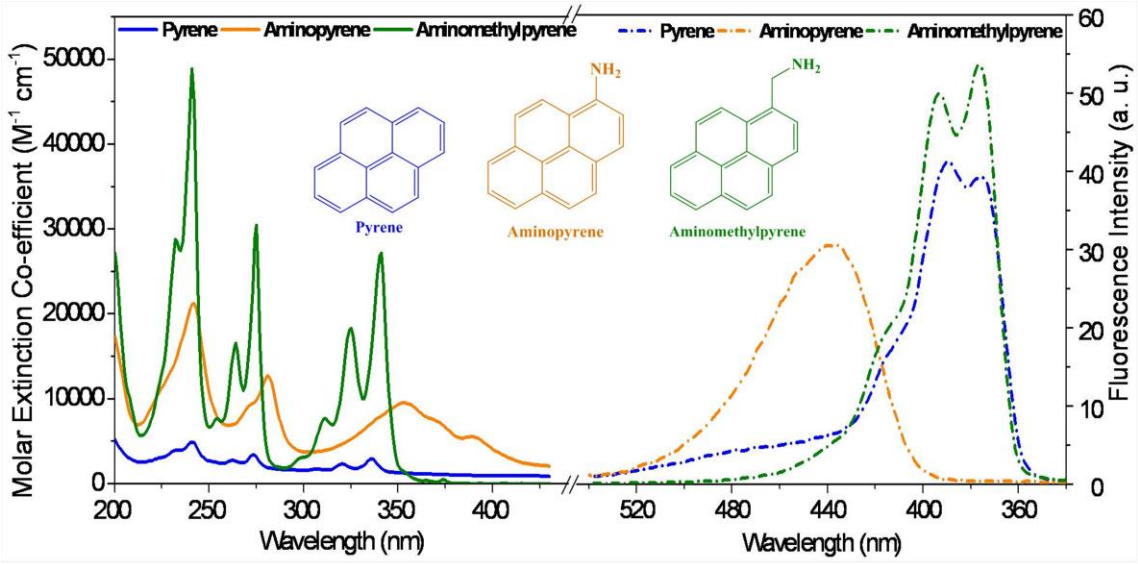

Figure 4.3. Absorption (25, 25 & 25 μM) and emission (0.3, 0.04 & 0.03 μM) spectra of pyrene, aminopyrene and aminomethylpyrene. Inset shows the molecular structures of the fluorescent probes.

study their emission behavior in varieties of microenvironments. The absorption and emission spectra of pyrene moieties, *viz.*, pyrene, aminopyrene and aminomethylpyrene are shown in Figure 4.3. The molecular structures of the fluorescent probes are shown in the inset. It is seen that the aqueous solution of pyrene and its derivatives possess well-defined absorption and emission bands (λ_{ex} ~ 274 nm) in the visible region which can be attributed to the monomeric form of the fluoroprobes.[22,32] The excitation of the fluoroprobes in any absorption maximum produces the identical emission spectrum. Moreover, the fluorescence intensity increases linearly with increasing concentration for all the three dye molecules indicating no significant perturbation or higher order aggregation in the experimental concentration range. The absorption and emission spectral features of the pyrene moieties are summarized in Table 4.2.

Table 4. 2. Absorption and Emission Spectral Characteristics of the Molecular Probes

Probes	Absorption maximum (nm)	Emission maximum (nm)	Quantum yield
Pyrene	241, 262, 273, 320, 336	375, 389	0.35 in ethanol
Aminopyrene	242, 281, 353, 389	438	0.58 in water
Aminomethylpyrene	240, 264, 274, 311, 325, 340	377, 394	–

Now, we have studied the emission behavior of pyrene and its derivatives (λ_{ex}~ 274 nm) in the presence of silver nanoparticles of four different sizes. The representative fluorescence spectrum of PY, APY and AMPY in the presence of 6 nm silver particles (set B) is shown in Figure 4. 4. In these experiments, quite dilute solutions (0.03-0.3 μM) have been used so as to minimize the effects of excitation attenuation and solution self-absorption (so-called 'trivial effects'). It is seen that the emission of pyrene moieties showed distinctly different profile in the presence of different concentrations of silver nanoparticles. The quenching of molecular fluorescence in the vicinity of metallic nanostructures could be treated by the model proposed by Weitz et al.[33] A fluoroprobe in the vicinity of a metallic nanostructure may be influenced by radiative and the non-radiative de-excitation rates involved in the fluorescence emission in a manner similar to the effect of a nearby macroscopic metallic surface.[7,34] Depending on its relative position and orientation with respect to the nanostructure, the fluoroprobe may experience an enhanced or suppressed electric field, leading to a higher or lower excitation rate, respectively, in comparison to a fluorophore in free space. In metal-fluoroprobe hybrid assemblies, the excitation of the electronic plasma resonance leads to an increase in the absorption rate. In addition, the emission intensity is strongly frequency dependent: not

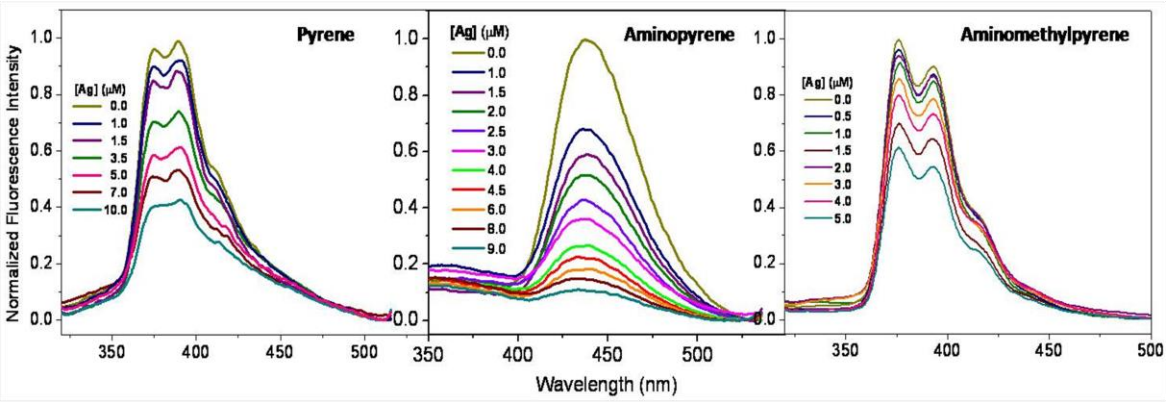

Figure 4.4. Fluorescence spectra of pyrene (0.3 μM), aminopyrene (0.04 μM) and aminomethylpyrene (0.03 μM) in the presence of variable concentrations of 6 nm silver nanoparticles.

only can the metal altered local photonic mode density lead to changes in the radiative decay rate of the fluorophores, but the presence of the metal also opens up new nonradiative decay pathways via energy transfer to metal surface plasmon modes.[35] In the

present experiment, it is observed that metallic nanostructures are efficient quenchers of molecular fluorescence while it is noted that the silver nanoparticles are, themselves, non-fluorescent. When the fluoroprobes are allowed to interact with the nanoparticles, a part of the fluoroprobes is adsorbed onto the metallic surface while the rests remain free in solution and thus, the only fluorescing components are the free pyrene moieties in the solution. The Stern-Volmer constant, K_{SV} is related to the photoluminescence efficiency via the relationship of the Stern-Volmer equation[36] accounting for both static and dynamic (collisional) quenching as,

$$\frac{I_0}{I} = 1 + K_{SV}[Q] \qquad (4.2)$$

where, I_0 and I are the intensities of the emission spectra of the pyrene moieties in the absence and presence of the nanostructures, $K_{SV} = K_S + K_D$, where, K_S and K_D are the

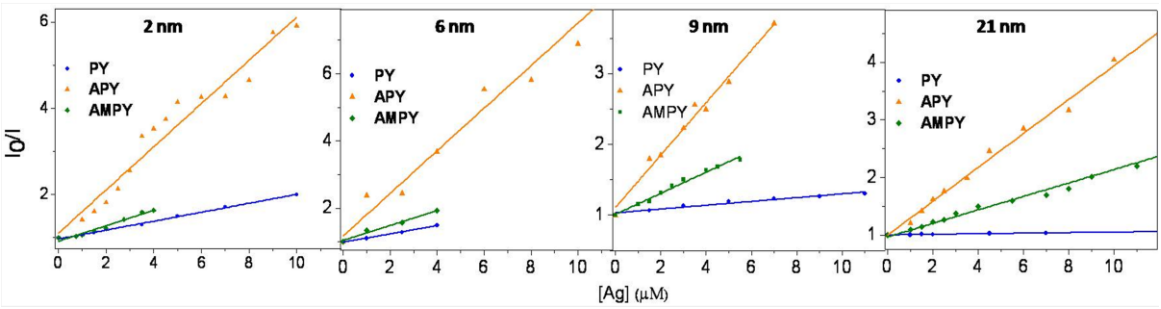

Figure 4.5. Stern-Volmer plots showing the quenching efficiency of pyrene (0.3 μM), aminopyrene (0.04 μM) and aminomethylpyrene (0.03 μM) in the presence of (A) 2, (B) 6, (C) 9 and (D) 21 nm silver nanoparticles.

static and dynamic quenching constants respectively and [Q] is the quencher concentration. Both static and dynamic quenching requires molecular contact between the fluorophore and quencher.[11] Figure 4.5 shows the profiles showing the relative efficiency, I_0/I as a function of silver concentration for all sets of the metallic nanostructures. It is also noted that the relative efficiency increases linearly with increase in the concentration of silver nanostructures. However, the salient feature of physical significance is that the extent of quenching is the least in case of pyrene, moderate for aminomethylpyrene and highest for the aminopyrene for all sets of particles. Moreover, smaller silver particles are efficient quenchers of molecular fluorescence than the larger ones as has been observed in previous investigations.[22]

Now, we have tried to elucidate the mechanism of quenching of molecular fluorescence upon interaction with the silver nanostructures. When using fluorescing molecules as local probes for measuring surface plasmon fields, we have to recall the particularities of molecular fluorescence near a metal surface. Both radiative and nonradiative decay rates are expected to depend, critically, on size and shape of the nanoparticle, the distance between the probe molecule and the nanoparticle, the orientation of the molecular dipole with respect to the fluoroprobe-nanoparticle axis, and the overlap of the molecule's emission with the nanoparticle's absorption spectrum.[37] In the vicinity of a metal, the fluorescence rate of molecules becomes a function of the

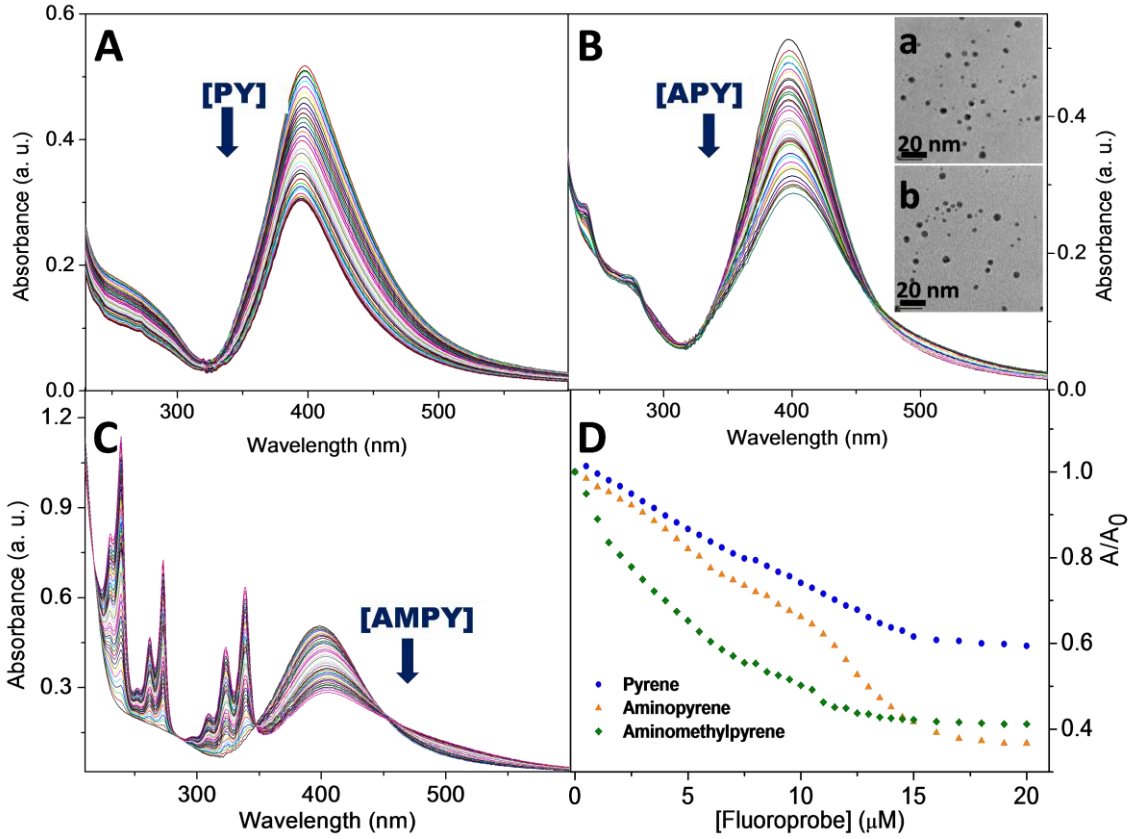

Figure 4.6. (A, B, C) Change in the surface plasmon band of 6 nm silver nanoparticles (50 μM) upon addition of pyrene (0.4 − 20 μM), aminopyrene (0.4 − 20 μM), and aminomethylpyrene (0.4 – 20 μM), respectively and (D) relative dampening of absorbance of the silver nanoparticles upon addition of fluoroprobes in different concentrations. Inset in profile B shows the transmission electron micrographs of the silver particles (set B) (a) before and (b) after addition of aminopyrene molecules.

distance between the molecule and the metal surface.[38] In direct contact with the metal, the fluorescence of molecules is completely quenched. While pyrene and its amine derivatives are added into the citrate-stabilized silver nanoparticles dispersion, one can speculate on the point of binding of the molecular probes to the metallic surface. Silver atoms at the surface of the particle are coordinately unsaturated, i. e., unoccupied orbitals are available for nucleophiles to donate electrons.[39] While the pyrene moieties are chemisorbed onto the surface of ultrasmall particles, the distance between the probe molecule and the nanoparticle, the orientation of the molecular dipole with respect to the fluoroprobe-nanoparticle axis could be assumed to remain constant and therefore, both electron and energy transfer processes are likely to contribute to the major deactivation pathways for excited fluoroprobes on the metal surface. Silver nanoparticles, themselves, show limited photoactivity under UV-visible irradiation, although photoinduced fusion and fragmentation have been observed under laser irradiation.[40] To examine the effect addition of pyrene and its two derivatives containing amine functional groups of the same homologous series on the surface plasmon absorption of the small metallic particulates, we have added the fluoroprobes to a particular concentration of the silver nanoparticles. Figure 4.6 shows the changes in the absorption spectral features of 6 nm silver nanoparticles (set B) (20 μM) upon successive addition of pyrene, aminopyerene and aminomethylpyrene molecules. It is seen that when pyrene moieties are added to the silver nanoparticles, the localized surface plasmon band of silver gradually dampens with increase in concentration of fluoroprobes (panel A─C); these results imply different extent of electron transfer from the fluoroprobes to the silver nanostructures.[39] Upon careful observation, it is observed that the LSPR maximum of the silver particles becomes blue shifted upon addition of PY, remains almost unchanged for APY and becomes red shifted for AMPY molecules. Inset in profile B shows the transmission electron micrographs of the silver particles (set B) before (panel a) and after (panel b) addition of aminopyrene which authenticate that the particle size remains nearly unchanged upon interaction with the probe molecules. A plot of A/A_0 as a function of fluoroprobe concentration (panel D) shows that the dampening of the silver surface plasmon band is the slowest for PY, intermediate for APY and the highest for AMPY. It is noted that after a critical concentration (15 μM), APY dampens the LSPR more

effectively than AMPY; however, after an incubation period of 12 h, APY more, actively, dampens the LSPR of the silver particles than AMPY at any concentrations.

The position and intensity of the silver surface plasmon absorption band depends strongly on particle size, and the optical and electronic properties of the medium surrounding the particles. This strong electronic interaction between pyrene moieties and silver particles causes the change in the surface plasmon band of the silver nanoparticles. The pyrene derivatives, *viz.*, aminopyrene and aminomethylpyrene containing amine functionality possess lone pair electrons capable of interacting with metal surface in competition with the stabilizing ligand shell, such as, citrate and therefore, can, in principle, displace the labile ligand, citrate on the surface of nanoparticles.[41] Donation of lone pair of electrons from the molecular probes to the nanoparticles causes a large reduction in absorption intensity of the silver particles. It is also possible that the fluoroprobes can displace citrate due to interaction of π-system of the molecule with the surface as well;[42] therefore, pyrene being an aromatic hydrocarbon and devoid of any functionality also dampens the plasmon oscillation of the metallic nanoparticles. The system of π-orbitals adjacent to the metal particles could have a weak interaction with the particle surface[43] and thus, shows little change in the absorption spectrum of the nanoparticles.[44] Another interesting feature is the high surface-to-volume ratio of the nanoparticles; higher the surface-to-volume ratio, stronger is the interaction with electron donating agents due to the co-ordinatively unsaturated surface atoms of the metals. The electron exchange from the PY to the Ag NPs or nucleophilic addition of APY and AMPY to Ag NPs leads to changes in the optical properties of the silver nanoparticles. Henglein and colleagues have shown that chemisorption of various nucleophiles has two opposing effects on the absorption spectra of colloidal silver.[45] When the electron transfer occurs to the metallic silver nanoparticles, the Fermi potential shifts to the more negative values corresponding the blue shift of the surface plasmon absorption band;[45] this has been observed when PY donates electrons to the surface of Ag NPs as seen in Figure 6A. The red shifting of the surface plasmon band of the Ag NPs is observed upon the nucleophilic addition of APY and AMPY to the Ag NPs as seen in Figure 6 (B and C). This may be explained by considering two opposing effects:[45] the number of charge increases in the particles which yield blue shift of the band and on the other hand, δ+ δ–

dipolar structure on the surface causes a red shift; when, the later effect was prevailing, red shift of the surface plasmon band is observed as has been seen for various silver-organic molecule systems.[46] However, since the lone pair of electrons on APY participate in resonance with its π-electrons in the pyrene ring, the extent of donation of lone pair of electrons is low compared to AMPY and there is no significant shifting of the absorption maximum of the silver surface plasmon band.

Cyclic voltammograms of pure fluoroprobes, silver nanoparticles (set B) and metal–fluoroprobe hybrid assemblies are shown in Figure 4.7. The observed anodic potentials (E_{pa}) are 100, 155 and 115 mV for PY, APY and AMPY, respectively while the corresponding cathodic potentials (E_{pc}) for metal-fluoroprobe hybrid assemblies are 600, 356 and 594 mV for Ag–PY, Ag–APY and Ag–AMPY, respectively. Therefore, the potential differences between the anodic peak of the pure fluoroprobes to the cathodic peak of silver-fluoroprobe hybrid assemblies (ΔE_P) are 503, 201 and 469 mV for PY, APY and AMPY molecules. This indicates that charge transfer takes place from the fluoroprobes to the silver nanoparticles, which reduces the potential differences between the fluoroprobes and silver–fluoroprobe hybrid assemblies.[47] Therefore, the less potential

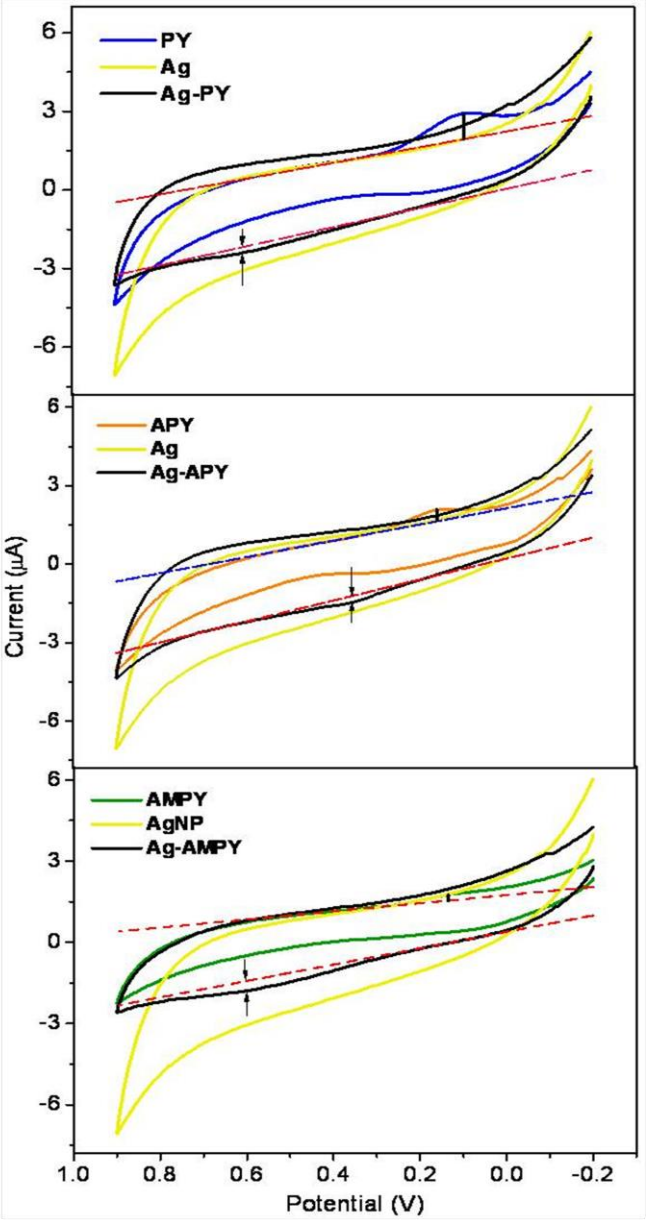

Figure 4.7. Cyclic voltammograms of the pure fluoroprobes (4.5 μM), silver nanoparticles (11.9 μM) and silver (11.9 μM)–fluoroprobe (4.5 μM) hybrid assemblies at pH~7.0.

difference value in case of APY indicates the facile electron transfer in Ag–APY hybrid systems as compared to Ag–PY and Ag–AMPY and follows the order Ag–APY > Ag–AMPY > Ag–PY. In addition, the current in the anodic and cathodic peaks of the probe molecules and the silver-fluoroprobe hybrids also signify the charge transfer from the fluoroprobes to the silver nanoparticles. In case of PY molecules, the anodic positive current (i_{pa} = 0.96 μA) decreases upon addition of Ag NPs and almost vanishes in Ag–PY hybrid systems rather develops a signature of negative current (i_{pa} = – 0.25 μA). Similar results have also been observed for Ag–APY (i_{pa}= 0.42 and –0.25 μA) and Ag–AMPY (i_{pa}= 0.24 and –0.38 μA) systems with peak shifting i. e., at different potential with a different current value. Therefore, from this observation, it is clear that anodic peak current is higher with the absence of cathodic peak current in pure fluoroprobes. But, upon addition of silver nanoparticles to form the silver-fluoroprobe hybrid assemblies, the anodic peak current is completely diminished with a signature of cathodic peak current (i_{pc} = –0.25, –0.25 and –0.38 μA). These phenomena also support the transfer of electrons from the fluoroprobes to the silver nanoparticles in the hybrid assemblies.[48]

In addition, if the donor molecule is placed in the vicinity of a conductive metal surface, resonance energy transfer takes place in which energy is transferred by a nonradiative, long-range dipole-dipole coupling from a fluorophore in an excited-state serving as a donor to another proximal ground state acceptor.[49,50] Förster resonance energy transfer (FRET) involves the nonradiative transfer of excitation energy from an excited donor to a ground state acceptor via resonance when brought in close proximity, which can radiatively emit a lower energy photon.[51] FRET processes are driven by dipole–dipole interactions and depend on the degree of spectral overlap between donor fluorescence and acceptor absorption, and on the sixth power of the separation distance between the donor and acceptor pair.[50] In the present experiment, the resonance energy transfer is believed to be through the dipole-dipole near-field interaction, where the fluorophores act as dipolar donors and the plasmonic silver nanostructures act as dipolar acceptors.[51] According to this formalism, the Förster distance, R_0, was calculated in which best distance resolution was exhibited below ~70 Å.[52] In the present experiment, the Förster distance, R_0, has been calculated approximately 29–33 Å for different nanoparticle–fluoroprobe assemblies. Therefore, Förster formalism could, exclusively, be

employed to explain the observed results. The probability of this Förster resonance energy transfer is proportional to the spectral overlap between the absorption of the metallic nanostructures and the fluorescence emission of the probe molecules.[53] The overlap integral, $J(\lambda)$ expresses the degree of spectral overlap between the donor emission and the acceptor absorption and can be written in terms of the following equation,[51]

$$J(\lambda) = \int_0^\infty F_D(\lambda)\varepsilon_A(\lambda)\lambda^4 d\lambda = \frac{\int_0^\infty F_D(\lambda)\varepsilon_A(\lambda)\lambda^4 d\lambda}{\int_0^\infty F_D(\lambda) d\lambda} \quad (4.3)$$

where, $F_D(\lambda)$ is the corrected fluorescence intensity of the donor in the wavelength range λ to $\lambda + \Delta\lambda$ with the total intensity (area under the curve) normalized to unity, $\varepsilon_A(\lambda)$ the extinction co-efficient of the acceptor at λ, which is typically in units of M^{-1} cm^{-1} and $F_D(\lambda)$ is dimensionless. If $\varepsilon_A(\lambda)$ is expressed in units of M^{-1} cm^{-1} and λ is in nanometers, then $J(\lambda)$ is in units of M^{-1} cm^{-1} nm^4. In calculating $J(\lambda)$, we could use the corrected emission spectrum with its area normalized to unity or normalize the calculated value of $J(\lambda)$ by the area; in this experiment, we have calculated the overlap integral by correcting the emission spectrum with its area normalized to unity. Figure 4.8 shows the spectral overlap between the absorption spectrum of 6 nm silver nanoparticles (set B) and the emission spectrum of PY, APY and AMPY ensuring efficient resonant

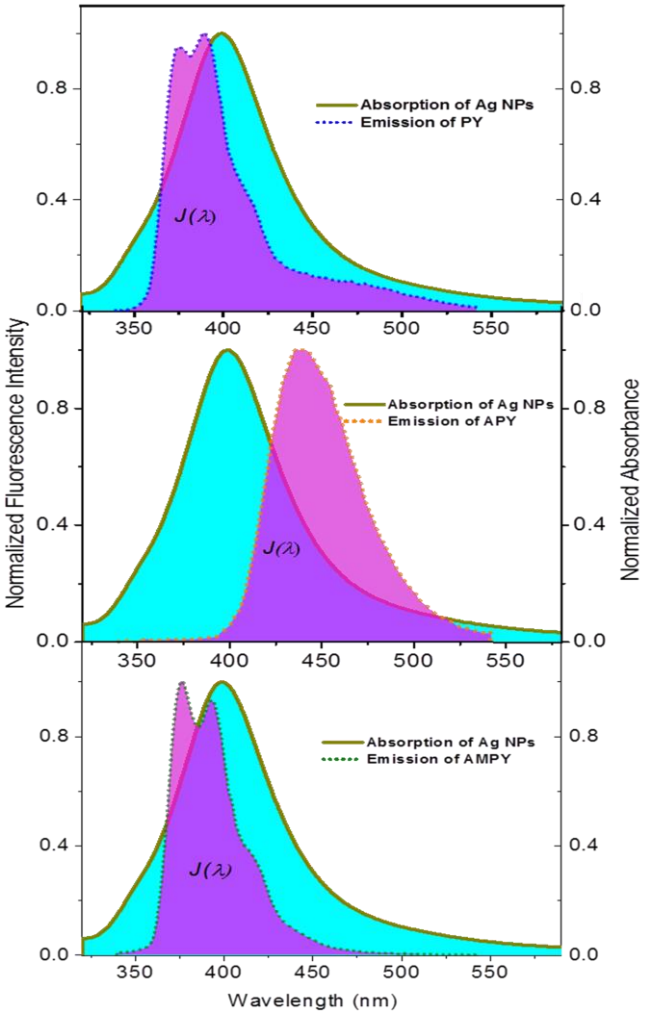

Figure 4.8. Overlap spectra of the emission spectrum of pyrene (0.3 μM), aminopyrene (0.04 μM), and aminomethylpyrene (0.03 μM) with the absorption spectrum of 6 nm Ag NPs (50 μM).

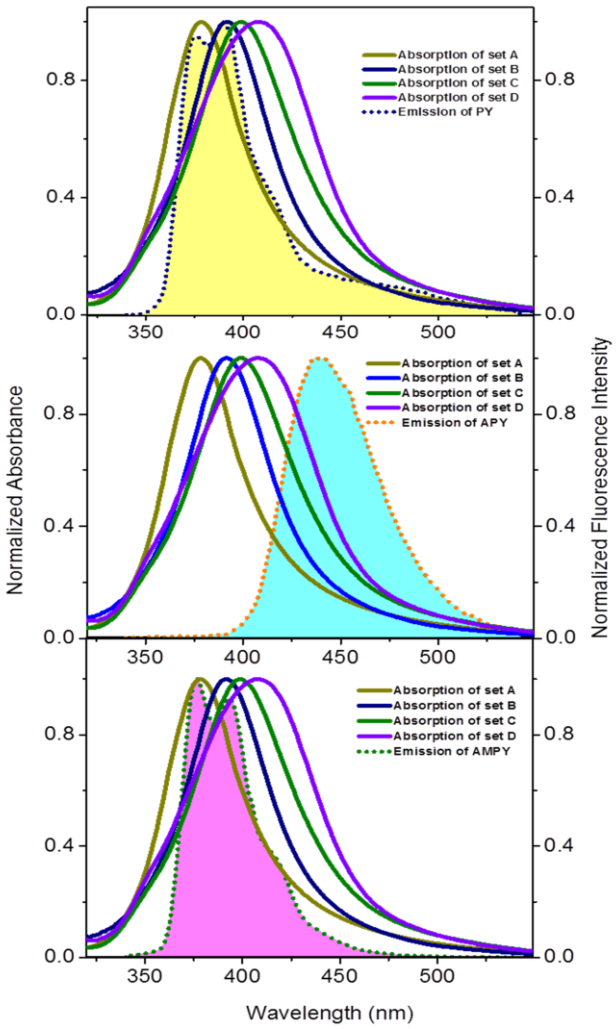

Figure 4.9. Overlap spectra of the emission spectrum of pyrene (0.3 μM), aminopyrene (0.04 μM) and aminomethylpyrene (0.03 μM) with 2, 6, 9 and 21 nm silver nanoparticles (50 μM).

energy transfer. It is seen that the LSPR of the silver nanoparticles has the maximum overlap with AMPY, lesser with PY and the least with APY which indicates AMPY could transfer energy more effectively than PY and APY molecules. The rate of Förster resonance energy transfer for a donor and acceptor separated by a distance r is given by,[51]

$$k_T(r) = \frac{Q_D k^2}{\tau_D r^6}\left(\frac{9000(ln10)}{128\pi^5 N_A \eta^4}\right)J(\lambda) \qquad (4.4)$$

where, Q_D is the quantum yield of the donor in the absence of acceptor, η the refractive index of the medium, N_A Avogadro's number, r the distance between the donor and acceptor and τ_D the lifetime of the donor in absence of acceptor. The term, κ^2 is a factor describing the relative orientation in space of the transition dipoles of the donor and acceptor; the value of $\kappa^2$is usually assumed to be 2/3, which is appropriate for dynamic random averaging of the donor and acceptor. Except overlap integral, since all the parameters are constants for a particular probe molecules, therefore, it is plausible to express to all the values in terms of overlap integral rather than the rate of energy transfer. To elucidate an explicit correlation between the fluorescence spectra of the molecular probes and the localized surface plasmon resonance spectra of the metallic nanoparticles, overlap spectra consisting of emission spectrum of PY or APY or AMPY and absorption spectra of four different sizes of silver

nanoparticles are presented in Figure 4.9. An account of related parameters in size-selective silver nanoparticle-induced fluorescence quenching of pyrene moieties are enunciated in Table 4.3. It is seen that the overlap integral, at first, increases and then, decreases with increase in particle

Table 4. 3. Account of Related Parameters in Silver Nanoparticle-Induced Fluorescence Quenching of Pyrene Moieties

AgNPs (nm)	Molecular probes	Overlap integral, J(λ)	K_{SV} (M^{-1})	K_{SV} (M^{-1})/ J(λ) (cm nm^{-4})	Mode of quenching	Observed quenching
	PY	2.2243×10^{14}	1.22×10^{5}	0.548×10^{-9}	FRET & ET	High
2±0.5	APY	1.0147×10^{14}	6.33×10^{5}	6.238×10^{-9}	FRET & ET	Very High
	AMPY	2.4728×10^{14}	2.21×10^{5}	0.894×10^{-9}	FRET & ET	High
	PY	1.9952×10^{14}	1.03×10^{5}	0.516×10^{-9}	FRET & ET	High
6±1	APY	1.3356×10^{14}	5.13×10^{5}	3.839×10^{-9}	FRET & ET	Very High
	AMPY	2.1914×10^{14}	1.82×10^{5}	0.830×10^{-9}	FRET & ET	High
	PY	1.5882×10^{14}	0.27×10^{5}	0.169×10^{-9}	FRET	Low
9±2	APY	1.2841×10^{14}	3.70×10^{5}	2.881×10^{-9}	FRET & ET	Very High
	AMPY	1.7332×10^{14}	1.47×10^{5}	0.848×10^{-9}	FRET & ET	High
	PY	1.1052×10^{14}	0.05×10^{5}	0.0425×10^{-9}	FRET	Very Low
21±3	APY	1.0492×10^{14}	2.94×10^{5}	2.802×10^{-9}	FRET & ET	High
	AMPY	1.1975×10^{14}	1.17×10^{5}	0.977×10^{-9}	FRET & ET	High

size with APY molecules that results from cumulative effect of gradual red shift (λ_{max} ~ 379 to 409) of the absorption maximum and decrease in extinction coefficient, $\varepsilon(\lambda)$ with increase in size of the particles. Moreover, it is noted that the overlap integral decreases for PY or AMPY molecules as the spectral overlap does not increase consequently with the red shift of the absorption maximum while extinction coefficient, $\varepsilon(\lambda)$ decreases with increase in size of the particles. The Stern-Volmer plots show that K_{SV} value decreases with increase in size of the Ag NPs. But, it is observed that for smaller nanoparticles (< 6 nm), K_{SV} values are very high even for pyrene molecules although it does not possess the capability of donating lone pair of electrons. A close inspection of K_{SV} values in Table 4.3 shows that K_{SV} increases in the sequence of PY<AMPY<APY irrespective of the particle size. Therefore, it is apparent that although APY has the less overlap integral values as

compared to PY and AMPY, the K_{SV} values are the highest for APY molecules. This phenomenon could be explicated in a substantial way by introducing a new parameter, differential quenching ($K_{SV}/J(\lambda)$, Stern-Volmer constant per unit overlap integral) to avoid all the plausible complications arising from the size of the metal particles, types of the molecular probes and difference in overlap integral values. Based on these perspectives, we have plotted the $K_{SV}/J(\lambda)$ values as a function of particle diameter of the Ag NPs for three different probe molecules as presented in Figure 4.10. From the graph, two important observations can be made. First, it is seen that, for larger particles (> 9 nm), APY and AMPY exhibit 60 to 20-fold higher $K_{SV}/J(\lambda)$ values, respectively, as compared to PY due the presence of $–NH_2$ and $–CH_2–NH_2$ functionalities, respectively. Second, for smaller Ag NPs (< 6 nm), the $K_{SV}/J(\lambda)$ values of PY is about 10-fold higher as compared to larger particles (> 9 nm) which supports the π electron transfer along with FRET to the Ag NPs. Similar results have also been observed for APY molecules, for which, $K_{SV}/J(\lambda)$ values are enhanced 2-fold as compared to

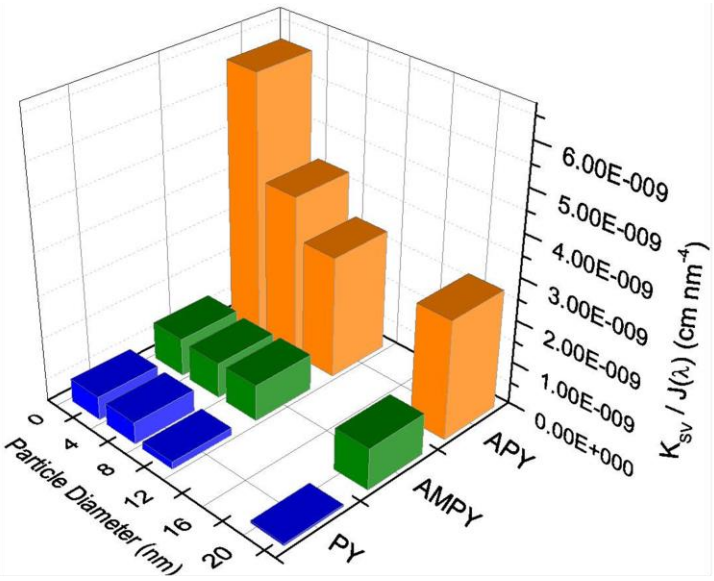

Figure 4.10. Differential quenching of pyrene moieties as a function of particle size of silver nanostructures.

Scheme 4.1. Schematic presentation of the possible deactivation pathways in silver-fluoroprobe hybrid assemblies.

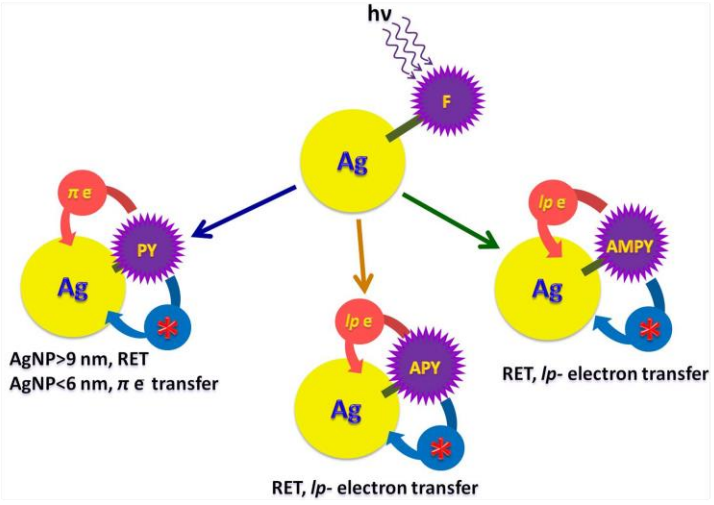

that of larger silver nanoparticles. Moreover, for smaller silver nanoparticles, $K_{SV}/J(\lambda)$ value is the highest (11- and 7-fold) for APY as compared to PY and AMPY molecules. Another important observation is that $K_{SV}/J(\lambda)$ values remain same for AMPY molecules irrespective of the size of the particles. From this experimental observation, it is apparent that the energy and electron transfer imbue explicit contributions in nanoparticle-induced fluorescence quenching and the extent of electron transfer is prominent for smaller (<6 nm) silver nanoparticles which is due to the pronounced residual force with decreasing the size of the particles. Based on these perspectives, a schematic presentation of the possible deactivation pathways in silver-fluoroprobe hybrid assemblies is enunciated in Scheme 4.1.

4.4. Conclusions

In conclusion, silver nanoparticles drastically alters the emission characteristics of pyrene and its amine derivatives that results from an invasive integration of the photophysical aspects of the molecular probes as well as the morphology and optical characteristics of the small metallic particulates. Thus, it is observed that fluorophore-bound silver nanostructures provide a convenient way to understand the surface binding properties of photoresponsive molecules and therefore, to examine the relative contributions of electron and energy transfer in the quenching processes. The new parameter, 'differential quenching' have been introduced that appear to realize individual electron and energy transfer in nanoparticle-induced fluorescence quenching. The consequence of physical interaction of nanoparticle-fluoroprobe assemblies provides strong evidence for the donation of both sigma and pi-electrons to the small metallic particulates. Probing the details of the mechanism can provide concrete empirical guidelines that can be used to more realistically in selecting ideal nanostructure-fluoroprobe quenching pairs for optical molecular rulers and optoelectronic nanodevices. We anticipate that experimental observation in the present investigation would pioneer future theoretical work in separating the electron and energy transfer contributions in nanoparticle-induced fluorescence quenching.

4.5. References

(1) Giannini, V.; Fernández-Domínguez, A. I.; Heck, S. C.; Maier, S. A. *Chem. Rev.* **2011**, *111*, 3888–3912.

(2) Ozbay, E. *Science* **2006**, *311*, 189−193.

(3) Ghosh, S. K.; Pal, T. *Phys. Chem. Chem. Phys.* **2009**, *11*, 3831–3844.

(4) Varnavski, O. P.; Ranasinghe, M.; Yan, X.; Bauer, C. A.; Chung, S. –J.; Perry, J. W.; Marder, S. R.; Goodson III, T. *J. Am. Chem. Soc.* **2006**, *128*, 10988–10989.

(5) Alvarez-Puebla, R.; Liz-Marzán, L. M.; F. de Abajo, J. G. *J. Phys. Chem. Lett.* **2010**, *1*, 2428–2434.

(6) Hobson, P. A.; Wedge, S.; Wasey, J. A. E.; Sage, I.; Barnes, W. L. *Adv. Mater.* **2002**, *14*, 1393–1396.

(7) Kamat, P. V.; Barazzouk, S.; Hotchandani, S. *Angew. Chem. Int. Ed.* **2002**, *41*, 2764–2767.

(8) Link, S.; El-Sayed, M. A. *J. Phys. Chem. B* **1999**, *103*, 8410–8426.

(9) Ghosh, S. K.; Pal, T. *Chem. Rev*. **2007**, *107*, 4797–4862.

(10) Stewart, M. E.; Anderton, C. R.; Thompson, L.B.; Maria, J.; Gray, S. K.; Rogers, J. A.; Nuzzo, R. G; *Chem. Rev.* **2008**, *108*, 494–521.

(11) Lakowicz, J. R. In *Principles of Fluorescence Spectroscopy*, 3rd edn., Plenum Press, New York, 2006.

(12) Dubertret, B.; Calame, M.; Libchaber, A. J. *Nat. Biotechnol.* **2001**, *19*, 365–370.

(13) George Thomas, K.; Kamat, P. V. *Acc. Chem. Res.* **2003**, *36*, 888–898.

(14) Maier, S. A. In *Plasmonics: Fundamentals and Applications* Springer-Verlag, USA, 2007.

(15) Rahman, D. S.; Ghosh, S. K. *Chem. Phys.* **2014**, *438*, 66–74.

(16) Jensen, T. R.; Malinsky, M. D.; Haynes, C. L.; Van Duyne, R. P. *J. Phys. Chem. B* **2000**, *104*, 10549–10556.

(17) Ni, W.; Ambjörnsson, T.; Apell, S. P.; Chen, H.; Wang, J. *Nano Lett.* **2010**, *10*, 77–84.

(18) Boal, A. K.; Rotello, V. M. *J. Am. Chem. Soc.* **2000**, *122*, 734–735.

(19) George Thomas, K.; Kamat, P. V. *J. Am. Chem. Soc.* **2000**, *122*, 2655–2656.

(20) Wang, T.; Zhang, D.; Xu, W.; Yang, J.; Han, R.; Zhu, D. *Langmuir* **2002**, *18*, 1840–1848.

(21) Ipe, B. I.; George Thomas, K.; Barazzouk, S.; Hotchandani, S.; Kamat, P. V. *J. Phys. Chem. B* **2002**, *106*, 18–21.

(22) Ghosh, S. K.; Pal, A.; Kundu, S.; Nath, S.; Pal, T. *Chem. Phys. Lett.* **2004**, *395*, 366–372.

(23) Evanoff, D. D. Jr.; Chumanov, G. *Chem. Phys. Chem.* **2005**, *6*, 1221–1231.

(24) Rahman, D. S.; Chatterjee, H.; Ghosh, S. K. *J. Phys. Chem. C* 2**015**, *119*, 14326–14337.

(25) Smart, L. E.; Moore, E. A. In *Solid State Chemistry: An Introduction* 3rd edn., Taylor & Francis, CRC Press: Boca Raton, Florida, USA, 2005.

(26) Liang, H.; Wang, W.; Huang, Y.; Zhang, S.; Wei, H.; Xu, H. *J. Phys. Chem. C* **2010**, *114*, 7427–7431.

(27) Li, S.; Shen, Y.; Xie, A.; Yu, X.; Qiu, L.; Zhang, L.; Zhang, Q. *Green Chem.* **2007**, *9*, 852–858.

(28) Offen, H. W. In *Organic Molecular Photophysics* Birks, J. B., Eds.; Wiley-Interscience, New York, 1975; Vol. 1.

(29) Förster, Th.; Kasper, K. *Z. Phys. Chem.* **1955**, *59*, 976–980.

(30) Kalyanasundaram, K.; Thomas, J. K. *J. Am. Chem. Soc.* **1977**, *99*, 2039–2044.

(31) Bertolotti, S. G.; Zimmerman, O. E.; Cosa, J. J.; Previtali, C. M. *J. Lumin.***1993**, *55*, 105–113.

(32) Kaur, M.; Kaur, P.; Dhuna, V.; Singh, S.; Singh. K. *Dalton Trans.* **2014**, *43*, 5707–5712.

(33) Weitz, D. A.; Garoff, S.; Gersten, J. I.; Nitzan, A. *J. Chem. Phys.* **1983**, *78*, 5324–5338.

(34) Kerker, M. *J. Colloid Interface Sci.***1985**, *105*, 297–314.

(35) Barnes, W. L. *J. Modern Opt.* **1998**, *45*, 661–699.

(36) Otto, S.; Volmer, M. *Phys. Z.***1919**, *20*, 183–188.

(37) Dulkeith, E.; Morteani, A. C.; Niedereichholz, T.; Klar, T. A.; Feldmann, J.; Levi, S. A.; van Veggel, F. C. J. M.; Reinhoudt, D. N.; Moller, M.; Gittins, D. I. *Phys. Rev. Lett.* **2002**, *89*, 2030021 1–4.

(38) Chance, R. R.; Prock, A.; Silbey, R. *Adv. Chem. Phys.* **1978**, *37*, 1–65.

(39) Makarova, O. V.; Ostafin, A. E.; Miyoshi Jr. H.; Norris, J. R.; Miesel, D. *J. Phys. Chem. B* **1999**, *103*, 9080–9084.

(40) Kamat, P. V.; Flumiani, M.; Hartland, G. V. *J. Phys. Chem. B* **1998**, *102*, 3123–3128.

(41) Puddephatt, R. J. In *Comprehensive Coordination Chemistry*; Wilkinson, G., Gillard, R. D., McCleverty, J. A., Eds.; Pergamon Press, Oxford, 1987; Vol. 5, pp. 862–891.

(42) Barradas, R, G.; Conaway, B. E. *J. Electroanal. Chem.***1963**, *6*, 314–325.

(43) Mohilur, D. M. In *Electroanalytical Chemistry* Bard, A. J. eds.; Marcello Dekker, New York, **1996**, Vol. 1, p. 355.

(44) Franzen, S.; Folmer, J. C. W.; Golm, W. R.; O'Neal, R. *J. Phys. Chem. A* **2002**, *106*, 6533–6540.

(45) Whitmore P. M.; Robata H. J.; Harris C. B. *J. Phys. Chem.* **1982**, *77*, 1560–1568.

(46) Henglein, A.; Mulvaney, P.; Linnert, T. *Faraday Discussion* **1991**, *92*, 31–44.

(47) Wu, Y.; Xu, W.; Wang, Y.; Yuan, Y.; Yuan, R. *Electrochim. Acta* **2013**, *88*, 135–140.

(48) Kerman, K.; Kobayashi, M.; Tamiya, E. *Meas. Sci. Technol.* **2004**, *15*, R1–R11.

(49) Kapoor, S. *Langmuir* **1998**, *14*, 1021–1025.

(50) Waldeck, H. J.; Alivisatos, A. P.; Harris, C. B. *Surf. Sci.***1985**, *158*, 103–125.

(51) Förster, T. *Ann. Phys.* **1948**, *437*, 55−75.

(52) Yun, C. S.; Javier, A.; Jennings, T.; Fisher, M.; Hira, S.; Peterson, S.; Hopkins, B.; Reich, N. O.; Strouse, G. F. *J. Am. Chem. Soc*. **2005**, *127*, 3115–3119.

(53) Hao, E.; Schatz, G. C. *J. Chem. Phys.* **2004**, *120*, 357–366.